

IDETC/CIE - 2021 71266

HYBRID MODELING OF MELT POOL GEOMETRY IN ADDITIVE MANUFACTURING USING NEURAL NETWORKS

Kevontrez Jones^{1,3}, Zhuo Yang^{2,3}, Ho Yeung⁴, Paul Witherell⁴, and Yan Lu^{*,4}

¹Northwestern University, Evanston, IL, USA

²University of Massachusetts Amherst, Amherst, MA, USA

³Associate at National Institute of Standards and Technology (NIST), Gaithersburg, MD, USA

⁴National Institute of Standards and Technology (NIST), Gaithersburg, MD, USA

ABSTRACT

Laser powder-bed fusion is an additive manufacturing (AM) process that offers exciting advantages for the fabrication of metallic parts compared to traditional techniques, such as the ability to create complex geometries with less material waste. However, the intricacy of the additive process and extreme cyclic heating and cooling leads to material defects and variations in mechanical properties; this often results in unpredictable and even inferior performance of additively manufactured materials. Key indicators for the potential performance of a fabricated part are the geometry and temperature of the melt pool during the building process, due to its impact upon the underlining microstructure. Computational models, such as those based on the finite element method, of the AM process can be used to elucidate and predict the effects of various process parameters on the melt pool, according to physical principles. However, these physics-based models tend to be too computationally expensive for real-time process control. Hence, in this work, a hybrid model utilizing neural networks is proposed and demonstrated to be an accurate and efficient alternative for predicting melt pool geometries in AM, which provides a unified description of the melting conditions. The results of both a physics-based finite element model and the hybrid model are compared to real-time experimental measurements of the melt pool during single-layer AM builds using various scanning strategies.

Keywords: Additive Manufacturing, Neural Networks, Melt Pool Dimension Prediction, Finite Element Method

1 Introduction

Metal additive manufacturing (AM) produces metallic parts by fusing materials in a layer-by-layer fashion directly from a 3D CAD model [1]. Laser powder bed fusion (L-PBF) is a common AM process in which a thin layer of metallic powder is spread on a substrate and a laser source selectively melts and fuses neighboring powder particles and the previous layer. This is repeated in a layer-by-layer fashion until the desired final part is formed. Since L-PBF has the potential to produce highly customizable parts with complex geometries and internal structures it has garnered great interest from the aerospace, automotive, and biomedical industries [2–4]. Despite offering these advantages and several others, L-PBF is known to struggle with producing parts which have reliable and repeatable mechanical performance due to inconsistencies in the microstructure [5]. However, recent studies prove both the microstructure and mechanical properties of parts produced through AM are significantly influenced by the size and shape of melt pool [6].

In L-PBF, the formation of the melt pool is the key to describing the powder-bulk material interactions because it is an intermediate step between solidification and laser source absorption [7]. This is because the localized solid powder heats up and melts into a liquid after absorbing energy from the passing laser, then cools down and solidifies into a bulk material with a result microstructure as the laser moves further away. For example, porosity in L-PBF may occur due to either improper melt pool formation from insufficient melting caused by too little energy absorption or trapped gas caused by vaporization and too much energy absorption [8, 9]. Much research has shown that energy absorption in AM can be traced in AM through a combination of process parameters such as laser power, scanning speed and

*Corresponding author: yan.lu@nist.gov

spot size, as well as the scanning strategy of the energy source. Hence, desired quality of a part fabricated from L-PBF may be achieved through controlling the melt pool by manipulating these processing parameters.

There have been many research efforts aimed at understanding the influence of different process parameters and material properties on part quality [10, 11]. These attempts with computational modeling and simulations have been used to explain relationships between process parameters and melt pool formation. Although, experiments are capable of directly capturing physical phenomena, they tend to be time consuming, expensive, and suffer from uncertainties due to inconsistencies in the process and errors with sensors [12]. Experimental data-driven modeling method is a straight forward and robust approach that has been widely used in AM domain [13, 14]. The predictive result, if well comply with the experimental conditions, can be used to optimize the L-PBF process with promised solution [15]. However, due to a lack of physical understanding in the model, the pure data-driven model is sensitive to these experimental conditions that are not part of the input variables. More specifically, the models are only applicable for unique scan strategies due to the manner in which they are constructed. Therefore, their predictions may significantly decrease in accuracy if a different scan strategy is implemented [16].

For these reasons, physics-based computational modeling has become a crucial complement to experimental investigations for understanding process-structure-property relations in AM [17]. For example, experiments and simulations have revealed that high energy input can produce larger melt pools when other parameters remain unchanged [18–21]. Hence, melt pools in AM are commonly manipulated by controlling the energy input of the system. In-situ control of the energy input may be easy, but melt pool formation may also be greatly affected by other factors which are extremely difficult and/or nearly impossible to control.

Environmental conditions and geometric variations are also known to affect melt pool shape and sizes [12]. For example, both simulations and experiments have proven that the presence of surfactants, such as oxygen, can change the shape of the melt pool by affecting its surface tension [22]. Additionally, the scan pattern also affects the shape and size of the melt pool due to heat transfer across adjacent tracks and/or layers [23, 24]. Due to all these potential parameters, the melt pool may vary both in time and space during the L-PBF process, which can detrimentally affect mechanical properties of the part. This has led researchers to investigate the influence the toolpath has on the melt pool geometry, in addition to the process parameters.

Several different types of models have been applied to investigate variations in the melt pool for multi-track and/or multi-layer builds. Two-dimensional [12] and semi-analytical models [25] can provide the variations in melt pool size for multi-track builds but they do so with limited fidelity. A two-dimensional

model cannot capture the full melt pool shape and semi-analytic models must neglect key physical phenomena in the AM process. High-fidelity, three-dimensional, models utilizing computational fluid dynamics have also been used to overcome these discrepancies [26–28]. However, when too much physics is considered the model's computational cost becomes too high to investigate the AM process at the part-scale. Therefore, these models tend to be limited to simulating very few layers and/or tracks with a short track length. On the contrary, models based on the finite element method (FEM) offer a desirable trade off between physics considered and feasible domain size to investigate tool paths and melt pools of an AM build.

Although, FEM models can provide a thermal history of an entire part being built [29–32], but they do so by purely considering heat conduction and neglecting the fluid flow behavior within the melt pool. This simplification can lead to predictions of inaccurate temperature fields if extensive calibrations are neglected. In order to overcome these disadvantages, while preserving the ability to make predictions on the part-scale at a low computational cost a hybrid model is presented. The hybrid model aims to utilize data analytic to both improve the accuracy and efficiency of physics-based simulations by intertwining computational and experimental data. Previous hybrid approaches demonstrated an improvement in both efficiency and accuracy using a small amount of experimental data by integrating it with physics-based simulations, but they did not consider the effects of the scan strategy [33, 34].

This work uses these ideas to investigate tool path design for the L-PBF process by combining numerical simulations and experiments to construct a hybrid model. This paper begins by describing the methodology of the study (Sec. 2). First the experimental procedure (Sec. 2.1) used to measurement attributes of the melt pool is provided. Second, the thermal model, based on FEM, of the L-PBF process is presented (Sec. 2.2), and followed by the description of the hybrid model (Sec. 2.3). Next, details the development and performance of the hybrid model by using variations in the surface area of the melt pool as a case study (Sec. 3). In order to do this, images from the experiments are converted to temperatures scales (Sec. 3.1) and compared against the FEM model (Sec. 3.2). Finally, the hybrid model is shown to reduce errors seen from both the initial FEM simulations and pure data-driven models (Sec. 3.3).

2 Methodology

An integrated computational and experimental approach is taken to model the L-PBF process for Inconel 625 (IN-625) alloys. Since we are interested in toolpath design, this paper focuses on the part scale. Experiments are used to record in-situ images of the melt pool under highly controlled conditions. In addition, the thermal dynamics for the same material and toolpaths are predicted using a physics-based model. Thereafter, a

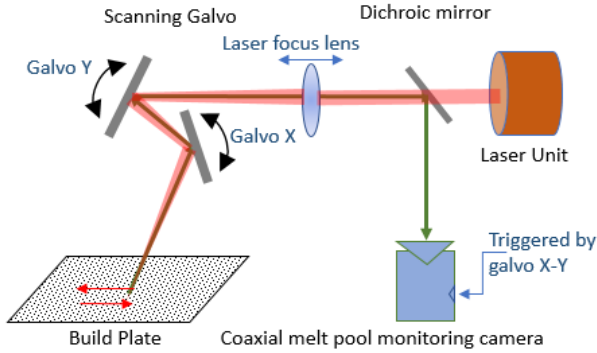


FIGURE 1: In-situ melt-pool image registration

hybrid model is constructed for which combines the two for improved predictive capabilities.

2.1 Experimental Set-Up

The experiments is conducted on The National Institute of Standards and Technology (NIST) Additive Manufacturing Metrology Testbed (AMMT) [35]. The NIST AMMT is a fully custom, open-platform laser powder bed fusion (LPBF) system to advance controls, monitoring, and metrology research. The in-house developed AM control software (SAM) allows the creation of various scan strategies from a simple combination of different scan strategies and laser power/speed control [15]. The melt-pool incandescent emission is diverted to a high-speed camera by a dichroic mirror and filtered at a bandwidth of (85 +/- 20) nm, as shown in Fig. 1. The custom optics enable 1:1 magnification and an image resolution of 8 μm/pixel. The camera is triggered by the laser position and hence the melt-pool image can be mapped to its location precisely.

Cubic Inconel 625 parts with the same design are built with different scan strategies. The design is shown in Fig. 2. The purpose of different corner chamfers is to give the part a distinctive orientation. The three scan strategies studied are: (a) constant build-speed with linear path (also known as skywrite), (b) Exact stop with island linear path, (c) Continuous with island spiral path. The nominal scan speed and laser power are 800 mm/s and 195 W respectively. Also a layer thickness of 20 μm, and an inter-layer rotation angle of 67° are applied.

2.2 Physics-based Modeling with FEM

A macro-scale thermal analysis is used to model the L-PBF process for a multi-track build. This analysis is done using a transient thermal Finite Element solver [36] to predict the global history for the laser traversing across a single layer of powder

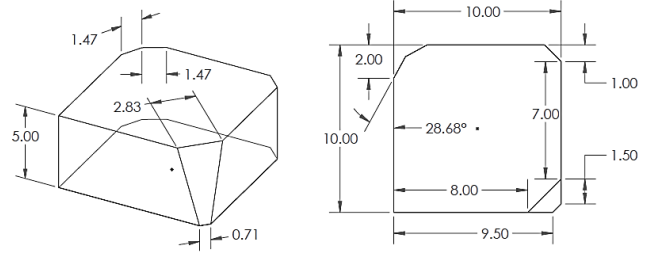


FIGURE 2: Part design (in mm)

covering a solid substrate. The governing heat transfer energy balance to be solved is:

$$\frac{\partial \rho c_p}{\partial t} = \frac{\partial}{\partial x_i} \left(k \frac{\partial T}{\partial x_i} \right) \quad (1)$$

where ρ is the material density, c_p is the specific heat, t is the time, x_i are the spatial coordinates, k is the conductivity of the material, and T is the temperature.

The moving laser in the L-PBF process is modeled as a heat source described by the Gaussian distribution:

$$q_{laser} = \frac{2P\eta}{\pi R_b^2} \exp \left(\frac{-2(x^2 + y^2 + z^2)}{R_b^2} \right) \quad (2)$$

where P is the power of the laser, η is an absorptivity factor to limit the amount of energy absorbed by the material from the laser which is taken to be 30 %, and R_b is the radius of the laser. The variables x , y , and z are local coordinates of the laser. Heat loss on the d free surfaces of the model is simulated though a combination of convection and radiation. Convective heat loss is defined by

$$q_{conv} = h_c (T - T_\infty) \quad (3)$$

where h_c is a convection coefficient, T is the surface temperatures, and T_∞ is the far-field (ambient) temperature. Radiation heat loss is defined using the Stefan-Boltzmann law, given by

$$q_{rad} = \sigma_s \varepsilon (T^4 - T_\infty^4) \quad (4)$$

where σ is the Stefan-Boltzmann constant and ε is the surface emissivity of the material.

Since this approach models the L-PBF process at the macro-scale, the powder layer is treated as a continuous media and it is distinguished from the substrate through its material properties.

This is achieved through the use of a consolidated factor, ϕ defined by the range of 0-1. The value of 0 denotes the material is in the original powder state (no consolidation), whereas 1 denotes a bulk state (fully consolidated). As seen from (5), ϕ is determined by temperature history, where T_{peak} is the local peak temperature, and $T_{solidus}$ and $T_{liquidus}$ are the material's solidus and liquidus temperatures respectively. It should be noted that through this definition ϕ solely increases monotonically.

$$\phi = \frac{T_{peak} - T_{solidus}}{T_{liquidus} - T_{solidus}} \quad (5)$$

Since ϕ denotes the state of the material at a given time, it is used to determine state-dependent effective material properties. By assuming a linear dependence, the effective material property, λ , is determined by (6), where λ_{bulk} and λ_{powder} are the appropriate material property for the powder and bulk solid. However, in this work it is assumed this relation only applies to the material's thermal conductivity and density.

$$\lambda = \lambda_{bulk}\phi + \lambda_{powder}(1 - \phi) \quad (6)$$

Based on prior research [37–39], it is assumed that the thermal conductivity of the powder is 2.1 W/m/k. However, the local density of the powder, ρ_{powder} , is determined by (7), where ψ is the powder packing (taken to be 50%), and ρ_{bulk} is the density of the bulk solid.

$$\rho_{powder} = \psi\rho_{bulk} \quad (7)$$

The build parameters, including laser speed and power and the toolpath, and the material are chosen based on the aforementioned experiments. By keeping these aspects consistent, comparisons between the simulations and experiments can be drawn confidently.

2.3 Hybrid Model Approach

Physics-based computational models can provide unlimited predictions at any location on the part based on general physical rules and simplified environmental conditions. The FEM model developed in this can be applied for any L-PBF machines as a universal approach by adjusting the constant parameters and input variables. However, the model cannot incorporate excluded parameters such as specific conditions in AM machines and powder material. Although these parameters are constant for the same AM machine, the machine-to-machine differences can cause significant variation in the results. The hybrid model aims to capture the effect generated by the hidden conditions which are not included in the FEM model.

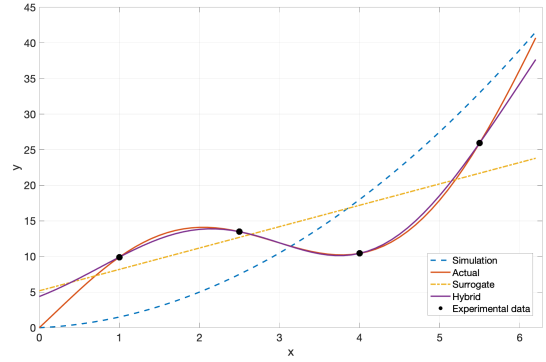


FIGURE 3: Example of hybrid modeling approach

Figure 3 shows an example of the hybrid modeling approach. The solid red curve is the actual model and the dashed blue curve is the simulation model. The solid dots represent the experimental data. The dashed yellow line is the surrogate model fit based on the four experimental data points using linear regression method. Due to the limited sample size, the experimental surrogate model fails to approach the actual curve. However, a hybrid model combining with the simulation and experimental data can accurately fit the actual curve. Instead of directly building a model by the given data points, the hybrid model focuses on calibrating the existing simulation by this additional information.

The grey-box modeling approach is used to build the hybrid model in this work [40]. The actual result can be represented as a combination of the simulated result and the error:

$$y_{exp} = y_{sim} + \varepsilon \quad (8)$$

where y_{exp} is the experimental measurement, which is assumed to be the ground truth in this work, y_{sim} is the simulated result, and ε is the corresponding error, which is defined as the residual. The term y_{sim} can be directly derived from:

$$y_{sim} = f_{sim}(x) \quad (9)$$

where $f_{sim}(x)$ represents the simulation model or the simulation-based surrogate model. A new dataset of the residual can be derived from calculating the error between every experimentally measured data point and the computationally predicted result. A surrogate model of the residual $\tilde{\varepsilon}$ can be presented as:

$$\tilde{\varepsilon} = f_{res}(x) \quad (10)$$

As a result, the final prediction is formulated by two components:

$$\tilde{y} = f_{sim}(x) + f_{res}(x) \quad (11)$$

As seen in Alg. 1, the hybrid modeling approach has 7 major steps. However, step 1 could be skipped if the simulation has low computational cost. In this study, the simulation-based surrogate model is generated to reduce the simulation time. The surrogate models in Step 1 and Step 6 both deploy the feed-forward neural network method [41].

Algorithm 1 Hybrid model construction

- Step 1: Build simulation-based surrogate model
 - Step 2: Design sampling method
 - Step 3: Collect measurement data from physical experiment
 - Step 4: Estimate the results by the same sampling method using simulation-based surrogate model
 - Step 5: Calculate the error between experimental and simulation result, $\epsilon = y_{exp} - y_{sim}$
 - Step 6: Build the surrogate model for the error using Eqn. (10)
 - Step 7: Build the hybrid model by combining the simulation-based and error surrogate models using Eqn. (11)
-

Figure 4 shows the neural network structure of the surrogate model in Step 6. The feed-forward neural network contains two hidden layers with 10 nodes for each. The neural network is fully connected with the Levenberg-Marquardt activation function. The x and y coordinates construct the input layer, and the residual $\tilde{\epsilon}$ is the final output. The simulation-based surrogate model deploys the same neural network structure and input variables, such that its results replaces the outputs of the physics-based simulation \tilde{y} . The neural network is trained by 80 % of data and tested by the other 20 %, and the Normalized Root Mean Square Error (NRMSE) is used to evaluate the performance of the model.

$$NRMSE = \frac{\sqrt{\sum_{i=1}^N (\tilde{y}_i - y_{exp,i})^2 / N}}{\bar{y}} \quad (12)$$

where i is the i^{th} data point and \bar{y} is the average measured value.

3 Case Study Results

To demonstrate some capabilities of the hybrid model, the surface of the melt pool visible to the laser is used as the output in this case study. Hence, this section details how the threshold of the experimental images are determined in order to ensure they contained the actual melt pool. The surface area, which varies both in time and space, of the melt pool is measured by an in-situ sensor using this threshold for three unique toolpaths. Then the aforementioned FEM model is employed and its predicted results

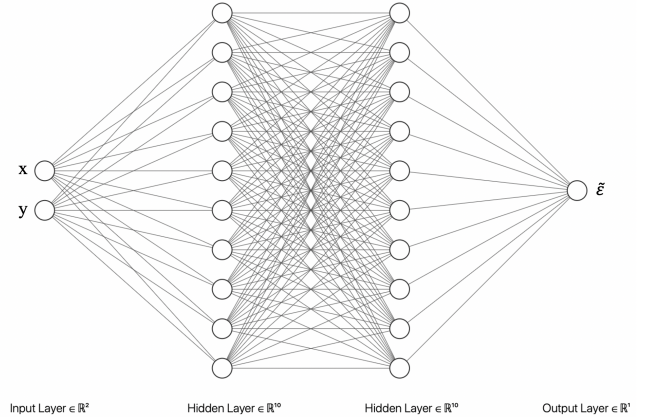


FIGURE 4: The neural network structure of $\tilde{\epsilon}$

are compared to the experiments for the same toolpaths. In order to reduce errors between the two, the hybrid model is employed and its error is compared to that of the FEM simulations.

3.1 Post-process analysis of Camera Images

The AMMT captures in-situ coaxial images during the build. The images are grayscaled from 0 to 255. Previous AMMT benchmark studies investigated the grayscale to temperature calibration [42, 43]. Figure 5 shows the calibration curve based on the preliminary findings [44]. Through implementing these procedures, the temperature measured from the thermal sensor was calibrated to the correlated optical grayscale value. Note, the minimum calibration measurement is for a grayscale of 5. A value lower than this would need to be extrapolated based on a fit to the available data. The grayscale is saturated at 255 with the relative temperature 1290°C.

The melting temperature of IN-625 is between 1290°C to 1350°C [45]. This study uses 1300°C to find the melt pool outline, with the relative grayscale equal to 10. This value is above the aforementioned minimum calibrated grayscale value of 5, and thus falls within the range of available measured data. The melt pool surface area is calculated by the enclosed area of the outline, where the scattering pixels would be removed in image pre-processing. Note, the curve is derived based on preliminary research findings. Therefore, it may suffer some uncertainties but it is believed to be adequate for this study. The same grayscale value to calculate the melt pool surface area is used for all cases. Hypothetically, it is appropriate to make parallel comparison between cases, but the calibrated temperature may not be accurate enough.

Figure 7 shows the three scan patterns studied in this work. All three cases use the same laser power (195 W) and scan speed (800 mm/s). Case 1 uses a skywrite approach with a traditional stripe pattern with an overshooting strategy. Here the overshoot-

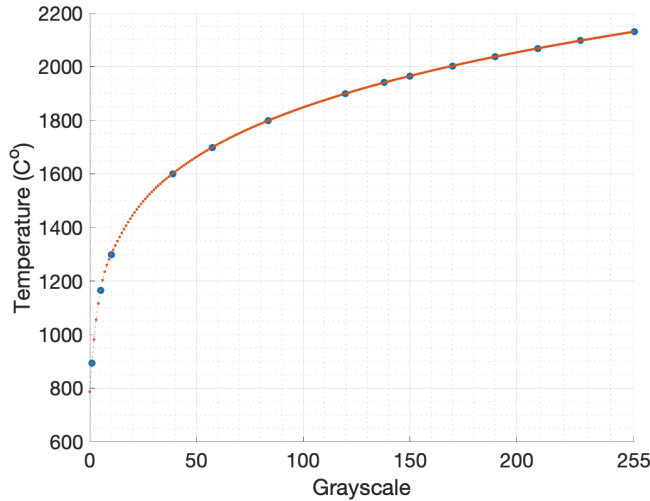


FIGURE 5: Grayscale to temperature calibration curve based on preliminary experimental result

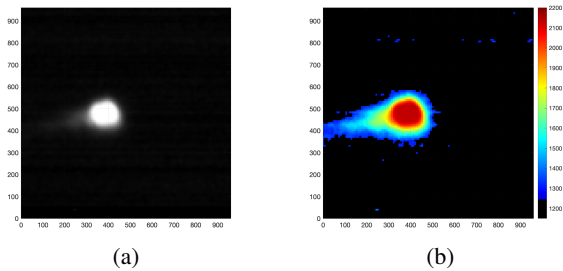


FIGURE 6: An example melt pool coaxial image calibrated from grayscale (a) to temperature (b)

ing indicates the laser beam continues to scan the area outside the part with zero laser power in order to maintain the same scan speed at the infilling area. Case 2 uses an island scan approach with linear paths and no overshooting. Whereas Case 3 uses an island scan approach, but with a spiral concentrating pattern. The no overshooting Case 2 and 3, due to the laser beam has to change direction within the infilling region, the scan speed would be operated to reduce and accelerate. This status would cause energy density vary in the infilling area but was captured by the simulation.

The frequency of the coaxial camera is 2000 Hz for all the cases. Therefore, the total number of images for each case depends on the laser scanning time. As a result, Case 1 to 3 collect 2661, 3884, and 6884 images, respectively.

3.2 FEM Simulation Results

The in-situ surface areas of the melt pool measured by the experiments are compared against the FEM model, shown by

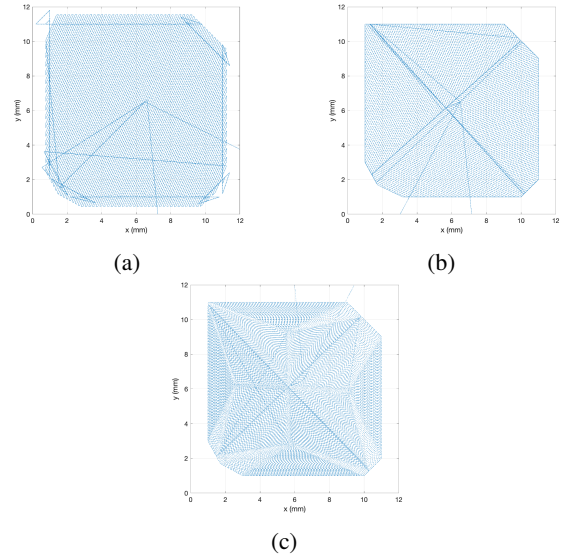


FIGURE 7: The complete scan patterns for Case 1 (a), Case 2 (b), and Case 3 (c). The green and red points are the start and end scanning position of the laser, respectively. The arrow points to the moving direction of the laser, where the skywriting (laser power = 0) path is also included

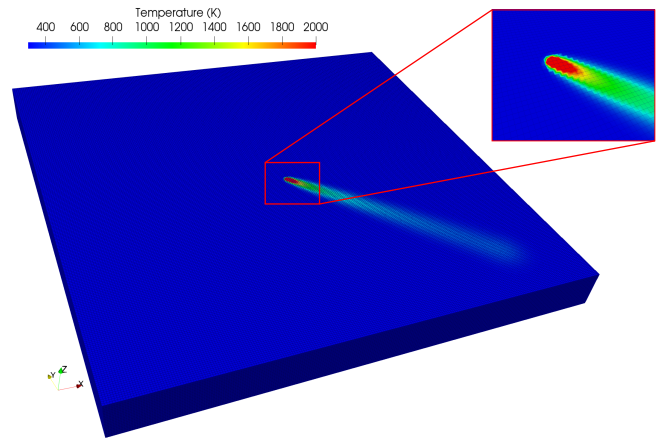


FIGURE 8: Example simulation of the L-PBF process from the FEM model. The effective powder layer was designed to be only one element thick, whereas the rest of the mesh in the depth mimicked the build plate.

Fig. 8, for the tool paths given by Fig. 7). This is done in the FEM model by calculating the surface area of the region above the solidus temperature at various time steps while the laser is nonzero. Since the time resolution of the camera in the experiments is 2000 Hz, data in the simulation is collected approximately every 50 μ s.

The simulations consisted of a computational domain of

12 mm x 12 mm x 1 mm with a fine mesh of 50 μm x 50 μm x 25 μm for the powder layer and surrounding area that the melt pool interacts with, and a slightly coarser mesh of 50 μm x 50 μm x 50 μm for the rest of the domain. All the simulations had about 1.3 million elements in total. Additionally, the thermophysical properties of IN-625 summarized in Table 1 are used. While all other properties are assumed to be constant, temperature-dependent polynomial functions are fitted to experimental measurements [46] of thermal conductivity and specific heat capacity.

Each surface area is approximated through a combination of a cubic interpolation and a convex hull. Using cubic interpolation the predicted temperature values from the top surface of the FEM model are mapped to a 2D grid with a grid spacing half that of the powder layer in the full-scale model. This ensures that the shape of the melt pool is well resolved. Then the surface area is calculated via a convex hull around the predicted melt pool region.

As seen by Fig. 9, the surface areas from the experiments and the simulations agree well qualitatively and provide similar trends. For Case 1, the surface area of the melt pool gradually increases in time. This is expected to occur when the dwell time between tracks is not small enough for the previous track to cool down before the laser starts melting the subsequent track. In this case, the residual heat within the previous track transfer to the new track and causes an increased size in the melt pool. Although the experimental measurements have a larger spread than the FEM model, they both show a linear relationship. Similarly, Case 2 also shows a linear relationship despite using an island scan approach. Although they provide similar trends, the experiments and simulations disagree with respect the rate at which the melt pool grows over time. For both cases, the numerically predicted rate is noticeably smaller than that of the experiments. However, one potential cause of this discrepancy could be noise in the data. Although the trends in the data are clear, for both cases the spread in experimental measurements is relatively large.

As noted by Fig. 9c, the trend in Case 3 is significantly different than that of the other two cases. Although, both Case 2 and Case 3 have an island scan strategy, the islands in Case 3 have less thermal interactions with each other. Due to this decrease of heat transfer across subsequent islands, the distribution of melt pool size is more representative by a single island.

3.3 Hybrid Model

To construct the hybrid model, each case first builds a simulation-based surrogate model to substitute the original simulation model to reduce the computational time. The testing dataset is used to validate both the simulation-based surrogate model and the hybrid model. Table 2 lists the NRMSE for the simulation-based surrogate model and the hybrid models of each

case. The tabulated results are consistent with Figure 9, since it states that the simulation of Case 3 has the lowest predictive error and Case 2 shows the highest. The hybrid model reduces the NRMSE to less than 1.0 for all cases. Though the final NRMSE for Case 3 drops to 0.0302 which denotes a 54.03 % improvement.

Figure 10 plots the contours of the melt pool surface areas for each case. The simulation-based surrogate model maps the melt pool area distribution over the layer. Case 1 accurately predicts the melt pool size gradually increases from the bottom right to the top left corner. It also shows the melt pool sizes close to the edge are smaller than those inside the build. Both the variation from island to island, and within the each island for Cases 2 and 3 are well predicted. However, the simulation lacks some details at some specific locations. For example, melt pool size of Case 1 from the simulation is generally higher than the experiment. Additionally, the bottom island of Case 2 does not completely match the experimental result. Plus the predicted melt pools at the edges of some islands do not agree well the experimental result. Case 3 shows a consistent trend of the evolution of melt pool size for the complex scan strategy, but it can be observed that the areas at center of the islands are under-predicted.

The hybrid model uses the training data to upgrade the original simulation-based surrogate model. It shows significant improvement for all cases, but is not perfect. The general melt pool sizes are reduced to match the actual sizes for Case 1. The inaccuracies within the island edge are corrected for Case 2. Lastly, predictions for Case 3 becomes significantly closer to the experimental measurements.

3.4 Performance of the hybrid model

The hybrid model can improve predictive accuracy by integrating the physics-based simulation and experimental data effectively. Previous models have demonstrated this capability, but unlike the model presented here, they lacked the ability to consider the scan strategy for an AM build citeyang2020scan. The simulations can generate an unlimited amount of data points if the computational time is acceptable. However, the cost of collecting in-situ experimental data for AM is exceedingly high. Therefore, a higher sampling rate would indicate a higher cost of the sensor and increased data processing. This increases the difficulties of conducting real-time process control for AM since the system would become overwhelmed with data. As a result, an ideal hybrid model should use a minimum amount of experimental data to provide the highest predictive accuracy.

This section designs a comparative study to investigate the impact of the sampling rate on the hybrid model's predictive accuracy. Each case selects 20 % evenly distributed data points from the experiment to be the fixed validation dataset. The remaining data constructs the training dataset. The hybrid model would partially utilize the training data to build the model, where

TABLE 1: Thermophysical properties of IN-625 used for the FEM simulations

Physical Property	Value	Source
Density (kg/m ³)	8440	[47]
Solidus temperature (K)	1563	[48]
Liquidus temperature (K)	1623	[48]
Specific heat capacity (J/kg/K)	$0.2437T + 338.39$	[46]
Thermal conductivity (W/m/K)	$0.0153T + 5.2366$	[46]
Latent heat of fusion (kJ/kg/K)	290	[47]

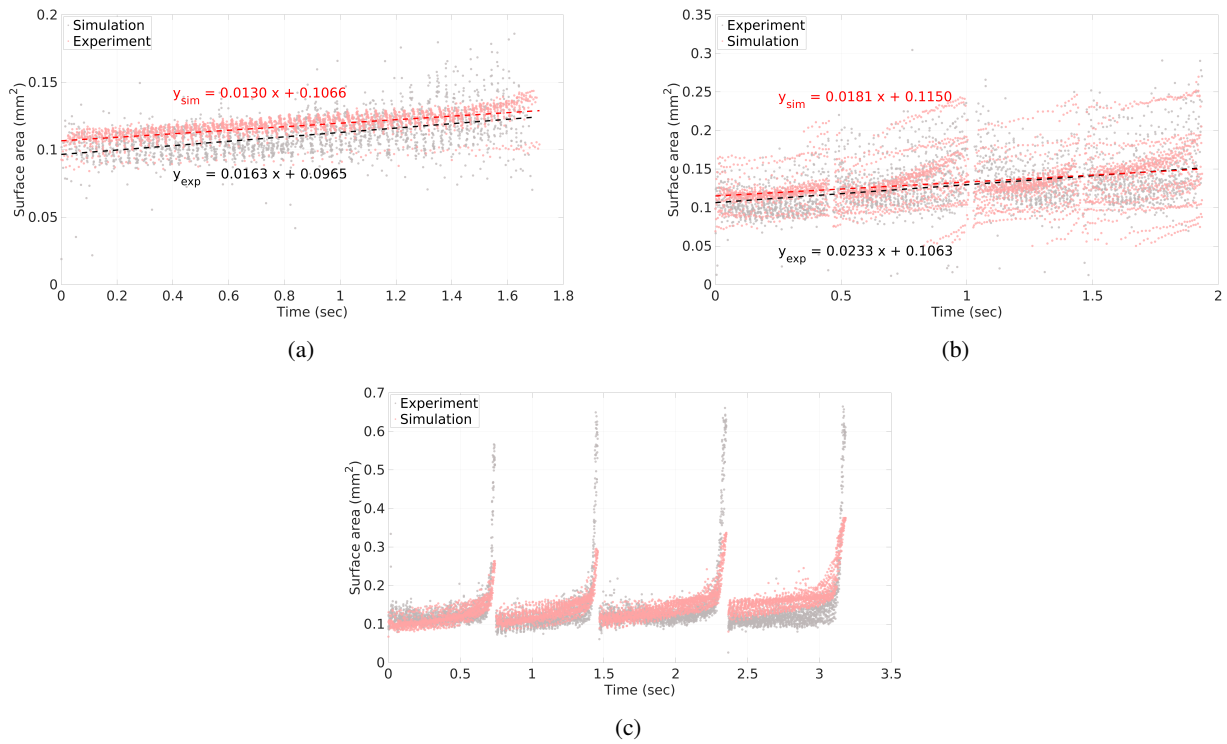


FIGURE 9: Comparisons of how the melt pool surface area evolves in time according to the experiments and simulations for Case 1 (a), Case 2 (b), and Case 3 (c)

TABLE 2: Model performance NRMSE of 3 cases by simulation-based surrogate model and hybrid model.

	Case 1	Case 2	Case 3
Simulation	0.1170	0.1258	0.0657
Hybrid	0.0821	0.1041	0.0302
Improvement	29.83 %	17.25 %	54.03 %

the simulation part keeps the same. The portion of the training data is from 10 % to 100 % with 5 % increment. For example, Case 1 has 2661 experimental data points. The training dataset has 2129 samples. The hybrid model with the least sample size would only use 213 data points. The picked points would be evenly distributed on the design space regardless to the sample size.

Figure 11 shows the NRMSE of each case with different sample size. Case 1 shows the NRMSE beyond 15 % has no sig-

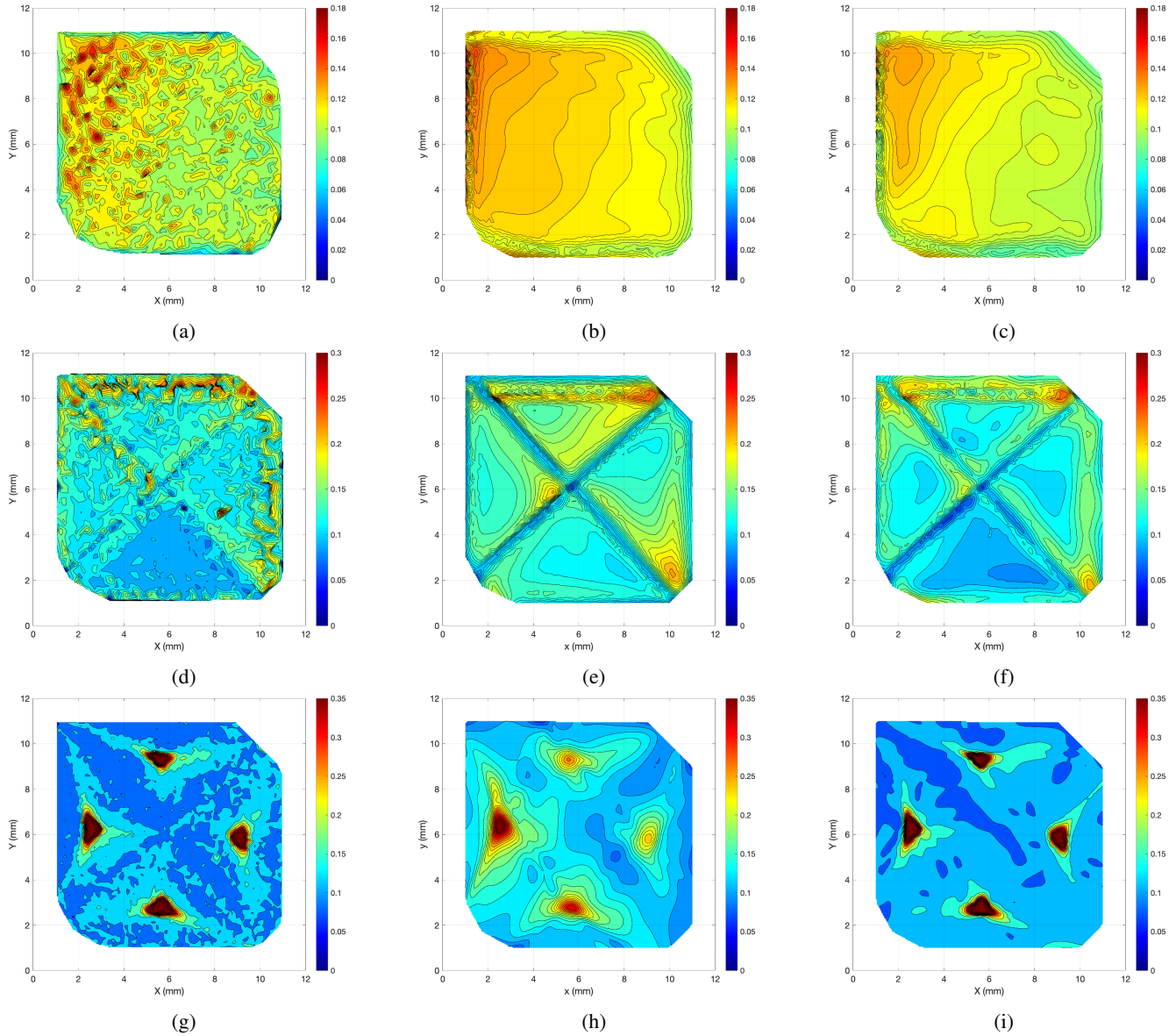


FIGURE 10: The contour plots of melt pool surface area for Case 1 (a-c), Case 2 (d-f), and Case 3 (g-i). Where the columns are results from experiments, FEM simulations and the hybrid modelling, respectively. The unit of the colorbar is mm^2

nificant difference. The final NRMSE at 100 % is 0.0811, which is close to the number reached at 15 % - 0.0839. However, the hybrid model increases sample size from 319 to 2129. Case 3 shows the similar result to Case 1, where the NRMSE approaches its converged point at 35 %. Considering the larger initial sample size (6884). It can reduce the sample size from 5507 to 2409.

Case 2 is more complicated that the increasing sample size can gradually reduce NRMSE from 0.1286 to 0.1041. However, the chart in Figure 9 shows a nearly flat curve between 40 % to 90 %. In addition, the total improvement for Case 2 is less than

0.03. The improvement introduced by the sample size seems not effective as there is no significant difference after sample size over 2409 as mentioned in previous paragraph.

4 Discussion and future work

The hybrid model in this paper solely uses simulation data from a heat conduction based model. Although the hybrid model proves to be more accurate than the initial FEM model for all the cases presented, this is partially based on the simulation-based

TABLE 3: Comparison of computational cost between the models for each case

	Num. Processors	Case 1	Case 2	Case 3
FEM simulation	24	848 min	1189 min	1419 min
Hybrid model	1	< 1min	< 1min	< 1min
Improvement	-	29.83 %	17.25 %	54.03 %

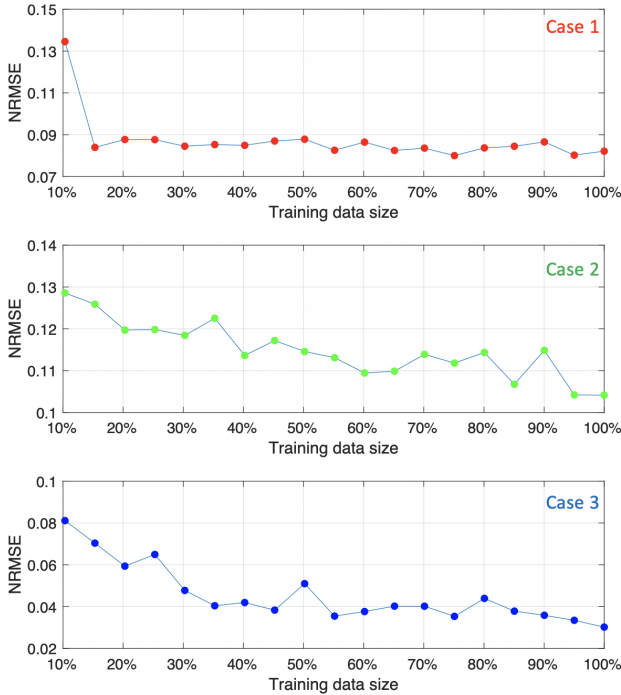


FIGURE 11: Performance of hybrid models with different training data size

surrogate model. In order to improve the accuracy of the hybrid model, the simulation-based surrogate model could include predictions from simulations which includes more physics. For example, a thermal-fluid model which incorporates the velocity field within the melt pool. However, such models tend to have a high computational cost so directly modeling the domains featured in this work would be difficult. The physics in the simulation can only capture the included parameters and variables. All deducted factors by the theoretical simplification would become uncertainties. Such factors could be powder quality, chamber temperature, substrate roughness, and laser instability. Those factors were ignored and have negative impact to the predictive accuracy.

The hybrid model only depends on a single material system as well, in this case IN-625. In addition to using predictions from

multiple physics-based models, the hybrid model could be generalized with transfer learning. Through transfer learning, the hybrid model would be able to combine a high volume of data from multiple sources and use it for new circumstances. In particular, it could use information from a database of experimental measurements for particular processing conditions and use it to better predict melt pool behavior for new ones. It is easy to generate simulation data for various process parameters and/or material systems, but with the help of prior knowledge from experimental measurements the hybrid model could ensure the predicted results are accurate.

5 Conclusion

In this work we demonstrate that a proposed hybrid model can be used to improve the accuracy of traditionally physics-based simulations for the L-PBF process and potentially expedite toolpath design. Initially, numerical results are predicted by a conduction-based FEM model and in-situ melt pool surface areas are measured from coaxial photography. The FEM model agrees well with the experimental observations qualitatively, but there are some quantitative discrepancies between the two.

In our approach, we attempt to reduce these discrepancies by constructing a hybrid model based on combining simulation-based and error-based surrogate models using data analytics. Each surrogate model is constructed by a feed-forward neural network. However, the simulation-based model uses data from the solely from the FEM simulations, whereas the error-based model uses data from both the experiment and FEM simulations. The performance of the hybrid model is demonstrated by comparing how well it predicts the spatially-varying surface areas for three toolpaths against the FEM results. It is proven that the hybrid model has less error than the FEM model with respect to the experimentally measured data. Due to this improved accuracy and computational efficiency, the hybrid model has potential applications in real-time toolpath planning.

In order to further improve the hybrid model's accuracy, data from additional simulations with higher fidelity models could be used. Through integrating data from experiments and multi-physics simulations, the hybrid model could be more extensible with respect to processing conditions. For example, a heat-

conduction model cannot capture key-hole mode behavior well. In this way, transfer learning could become very applicable. This work uses a feed-forward neural network in order to construct the simulation-based surrogate model and the error-based surrogate model. Through the use of transfer learning, the model would be able to use prior-obtained knowledge to predict aspects of the AM process for new circumstances, such as a new material system. This ability would be immensely beneficial for process control in AM.

Acknowledgment

For this work, K. Jones acknowledge the support by Northwestern University under the Walter P. Murphy Fellowship and the National Institute of Standards and Technology (NIST) under Cooperative Agreement number NIST 70NANB17H283.

Disclaimer

Certain commercial systems are identified in this paper. Such identification does not imply recommendation or endorsement by NIST; nor does it imply that the products identified are necessarily the best available for the purpose. Further, any opinions, findings, conclusions, or recommendations expressed in this material are those of the authors and do not necessarily reflect the views of NIST or any other supporting U.S. government or corporate organizations.

REFERENCES

[1] Bourell, D., Beaman, J., Marcus, H., and Barlow, J., 1990. "Solid freeform fabrication: An advanced manufacturing approach". In International Solid Freeform Fabrication Symposium, pp. 1–7.

[2] Vojislav, P., Juan, V. H. G., Olga, J. F., Javier, D. G., Jose, R. B. P., and Luis, P. G., 2011. "Additive layered manufacturing: sectors of industrial application shown through case studies". *International Journal of Production Research*, **49**(4), pp. 1061–1079.

[3] Yan, C., Hussein, A., and Raymont, D., 2012. "Evaluations of cellular lattice structures manufactured using selective laser melting". *International Journal of Machine Tools and Manufacture*, **62**, pp. 32–38.

[4] Guo, N., and Leu, M. C., 2013. "Additive manufacturing: technology, applications and research needs". *Frontiers of Mechanical Engineering*, **8**(3), pp. 215–243.

[5] Bourell, D., Leu, M., and Rosen, D., 2009. *Roadmap for additive manufacturing-Identifying the future of freeform processing*. The University of Texas at Austin, Laboratory for Freeform Fabrication, Advanced Manufacturing Center.

[6] Liu, Y., Li, S., Wang, H., Hou, W., Hao, Y., Yang, R., Sercombe, T., and Zhang, L., 2016. "Microstructure, de-

fects and mechanical behavior of beta-type titanium porous structures manufactured by electron beam melting and selective laser melting". *Acta Materialia*, **113**, pp. 56–67.

[7] Witherell, P., Feng, S. C., Martukanitz, R., Simpson, T. W., John, D. B., Michaleris, P., Liu, Z.-k., and Chen, L.-q., 2014. "Toward metamodelling for composable and reusable additive manufacturing process models". In 34th Computers and Information in Engineering Conference, Proceedings of the ASME Design Engineering Technical Conference, American Society of Mechanical Engineers (ASME). 061025.

[8] Cunningham, R., Narra, S. P., Montgomery, C., Beuth, J., and Rollett, A. D., 2017. "Synchrotron-based x-ray microtomography characterization of the effect of processing variables on porosity formation in laser power-bed additive manufacturing of ti-6al-4v". *JOM*, **69**(3), pp. 479–484.

[9] Tang, M., Postorius, P. C., and Beuth, J. L., 2017. "Prediction of lack-of-fusion porosity for powder bed fusion". *Additive Manufacturing*, **14**, pp. 39–48.

[10] Read, N., Wang, W., Essa, K., and Attallah, M. M., 2015. "Selective laser melting of als10mg alloy: Process optimisation and mechanical properties development". *Materials & Design*, **65**, pp. 417–424.

[11] Criales, L. E., Arisoy, Y. M., and Özel, T., 2016. "Sensitivity analysis of material and process parameters in finite element modeling of selective laser melting of inconel 625". *The International Journal of Advanced Manufacturing Technology*, **86**(9), pp. 2653–2666.

[12] Criales, L. E., Arisoy, Y. M., Lane, B., Moylan, S., Donmez, A., and Özel, T., 2017. "Laser powder bed fusion of nickel alloy 625: Experimental investigations of effects of process parameters on melt pool size and shape with spatter analysis". *International Journal of Machine Tools and Manufacture*, **121**, pp. 22–36.

[13] Yang, Z., Lu, Y., Yeung, H., and Krishnamurty, S., 2020. "From scan strategy to melt pool prediction: A neighboring-effect modeling method". *Journal of Computing and Information Science in Engineering*, **20**(5).

[14] Yang, Z., Eddy, D., Krishnamurty, S., Grosse, I., Denno, P., and Lopez, F., 2016. "Investigating predictive metamodelling for additive manufacturing". In International Design Engineering Technical Conferences and Computers and Information in Engineering Conference, Vol. 50077, American Society of Mechanical Engineers, p. V01AT02A020.

[15] Yeung, H., Lane, B., Donmez, M., Fox, J., and Neira, J., 2018. "Implementation of advanced laser control strategies for powder bed fusion systems". *Procedia Manufacturing*, **26**, pp. 871–879. 46th SME North American Manufacturing Research Conference, NAMRC 46, Texas, USA.

[16] Yang, Z., Lu, Y., Yeung, H., and Krishnamurty, S., 2020. "3d build melt pool predictive modeling for powder bed fusion additive manufacturing". In International Design En-

- gineering Technical Conferences and Computers and Information in Engineering Conference, Vol. 83983, American Society of Mechanical Engineers, p. V009T09A046.
- [17] Hu, Z., and Mahadevan, S., 2017. “Uncertainty quantification and management in additive manufacturing: current status, needs, and opportunities”. *The International Journal of Advanced Manufacturing Technology*, **93**(5), pp. 2855–2874.
- [18] Lu, Y., Yang, Z., Eddy, D., and Krishnamurty, S., 2018. “Self-improving additive manufacturing knowledge management”. In *Asme 2018 international design engineering technical conferences and computers and information in engineering conference*, American Society of Mechanical Engineers Digital Collection.
- [19] Thijs, L., Verhaeghe, F., Craeghs, T., Humbeeck, J. V., and Kruth, J.-P., 2010. “A study of the microstructural evolution during selective laser melting of ti-6al-4v”. *Acta Materialia*, **58**(9), pp. 3303–3312.
- [20] Lopez, F., Witherell, P., and Lane, B., 2016. “Identifying uncertainty in laser powder bed fusion additive manufacturing models”. *Journal of Mechanical Design*, **138**(11).
- [21] Huessein, A., Hao, L., Yan, C., and Everson, R., 2013. “Finite element simulation of the temperature and stress fields in single layers built without-support in selective laser melting”. *Materials & Design*, **52**, pp. 638–647.
- [22] Gan, Z., Yu, G., He, X., and Li, S., 2017. “Surface-active element transport and its effect on liquid metal flow in laser-assisted additive manufacturing”. *International Communications in Heat and Mass Transfer*, **86**, pp. 206–214.
- [23] Beal, V. E., Erasenthiran, P., Hopkinson, N., Dickens, P., and Ahrens, C. H., 2006. “The effect of scanning strategy on laser fusion of functionally graded h13/cu material”. *The International Journal of Advanced Manufacturing Technology*, **30**(9), pp. 844–852.
- [24] Liu, C., Tian, X., Tang, H., and Wang, H., 2013. “Microstructural characterization of laser melting deposited ti-5al-5mo-5v-1cr-1fe near β titanium alloy”. *Journal of Alloys and Compounds*, **572**, pp. 17–24.
- [25] Plotkowski, A., Kirka, M., and S.S., B., 2017. “Verification and validation of a rapid heat transfer calculation methodology for transient melt pool solidification conditions in powder bed metal additive manufacturing”. *Additive Manufacturing*, **18**, pp. 256–268.
- [26] Dubrov, A., Mirzade, F., Dubrov, V., and Rodin, P., 2018. “Numerical simulation of thermal behavior for process parameters optimization in laser additive manufacturing”. In *3D Printed Optics and Additive Photonic Manufacturing*, Vol. 10675, International Society for Optics and Photonics, SPIE, pp. 136–143.
- [27] Dubrov, A., Mirzade, F., and Dubrov, V., 2019. “On modeling of heat transfer and molten pool behavior in multi-layer and multi-track laser additive manufacturing process”. In *Modeling Aspects in Optical Metrology VII*, Vol. 11057, International Society for Optics and Photonics, SPIE, pp. 374–382.
- [28] Manvatkar, V., De, A., and DebRoy, T., 2015. “Spatial variation of melt pool geometry, peak temperature and solidification parameters during laser assisted additive manufacturing process”. *Materials Science and Technology*, **31**(8), pp. 924–930.
- [29] Lin, S., Smith, J., Liu, W. K., and Wagner, G., 2017. “An energetically consistent concurrent multiscale method for heterogeneous heat transfer and phase transition applications”. *Computer Methods in Applied Mechanics and Engineering*, **315**, pp. 100–120.
- [30] Wolff, S., Lin, S., Faierson, E. J., Liu, W. K., Wagner, G., and Cao, J., 2017. “A framework to link localized cooling and properties of directed energy deposition (ded)-processed ti-6al-4v”. *Acta Materialia*, **132**, pp. 106–117.
- [31] Romano, J., Ladani, L., and Sadowski, M., 2015. “Thermal modeling of laser based additive manufacturing processes within common materials”. *Procedia Manufacturing*, **1**, pp. 238–250.
- [32] Li, Y., and Gu, D., 2014. “Parametric analysis of thermal behavior during selective laser melting additive manufacturing of aluminum alloy powder”. *Materials & Design*, **63**, pp. 856–867.
- [33] Moges, T., Yang, Z., Jones, K., Feng, S., Witherell, P., and Lu, Y. “Hybrid modeling approach for melt pool prediction in laser powder bed fusion additive manufacturing”. In *ASME 2020 International Design Engineering Technical Conferences and Computers and Information in Engineering Conference*, American Society of Mechanical Engineers Digital Collection.
- [34] Mondal, S., Gwynn, D., Ray, A., and Basak, A., 2020. “Investigation of melt pool geometry control in additive manufacturing using hybrid modeling”. *Metals*, **10**(5), p. 683.
- [35] Lane, B., Mekhontsev, S., Grantham, S., Vlasea, M., Whiting, J., Yeung, H., Fox, J., Zarobila, C., Neira, J., Mcglauflin, M., Hanssen, L., Moylan, S., Donmez, M., and Rice, J., 2016. “Design, developments, and results from the nist additive manufacturing metrology testbed (ammt)”. In *Solid Freeform Fabrication Symposium*, Austin, TX, pp. 1145–1160.
- [36] Smith, J., Xiong, W., Cao, J., and Liu, W. K., 2016. “Thermodynamically consistent microstructure prediction of additively manufactured materials”. *Computational Mechanics*, **57**(3), pp. 359–370.
- [37] Rizal Alkahari, M., Furumoto, T., Ueda, T., Hosokawa, A., Tanaka, R., and Abdul Aziz, M. S., 2012. “Thermal conductivity of metal powder and consolidated material fabricated via selective laser melting”. *Key Engineering Materials*, **523-524**, pp. 244–249.
- [38] Rombouts, M., Froyen, L., Gusarov, A. V., Bentefour,

- E. H., and Glorieux, C., 2005. “Photopyroelectric measurement of thermal conductivity of metallic powders”. *Journal of Applied Physics*, **97**(2), p. 024905.
- [39] Childs, T., Hauser, C., and Badrossamay, M., 2005. “Selective laser sintering (melting) of stainless and tool steel powders: Experiments and modelling”. *Proceedings of the Institution of Mechanical Engineers, Part B: Journal of Engineering Manufacture*, **219**(4), pp. 339–357.
- [40] Yang, Z., Eddy, D., Krishnamurty, S., Grosse, I., Denno, P., Lu, Y., and Witherell, P., 2017. “Investigating grey-box modeling for predictive analytics in smart manufacturing”. In ASME 2017 International Design Engineering Technical Conferences and Computers and Information in Engineering Conference, American Society of Mechanical Engineers Digital Collection. V02BT03A024.
- [41] Svozil, D., Kvasnicka, V., and Pospichal, J., 1997. “Introduction to multi-layer feed-forward neural networks”. *Chemometrics and intelligent laboratory systems*, **39**(1), pp. 43–62.
- [42] Zhirnov, I., Mekhontsev, S., Lane, B., Grantham, S., and Bura, N., 2020. “Accurate determination of laser spot position during laser powder bed fusion process thermography”. *Manufacturing Letters*, **23**, pp. 49–52.
- [43] Heigel, J. C., Lane, B., Levine, L., Phan, T., and Whiting, J., 2020. “In situ thermography of the metal bridge structures fabricated for the 2018 additive manufacturing benchmark test series (am-bench 2018)”. *JOURNAL OF RESEARCH OF THE NATIONAL INSTITUTE OF STANDARDS AND TECHNOLOGY*, **125**.
- [44] Lane, B., and Yeung, H., 2020. “Process monitoring dataset from the additive manufacturing metrology testbed (ammt): Overhang part x4”. *Journal of Research of the National Institute of Standards and Technology*, **125**, pp. 1–18.
- [45] Arafin, M., Medraj, M., Turner, D. P., and Bocher, P., 2007. “Transient liquid phase bonding of inconel 718 and inconel 625 with bni-2: Modeling and experimental investigations”. *Materials Science and Engineering: A*, **447**(1-2), pp. 125–133.
- [46] Corporation, S. M., 2013. Inconel alloy 625. Tech. rep., Precision Castparts Corporation, August. <http://www.Specialmetals.com>.
- [47] Capriccioli, A., and Frosi, P., 2009. “Multipurpose ansys fe procedure for welding processes simulation”. *Fusion engineering and Design*, **84**(2), pp. 546–553. Proceeding of the 25th Symposium on Fusion Technology.
- [48] Pawel, R., and Williams, R., 1985. Survey of physical property data for several alloys. Tech. rep., Oak Ridge National Laboratory.